Elastic immersive wave experimentation

Geophysical Journal International

Geophys. J. Int. (2023) **233,** 724–739
Advance Access publication 2022 December 02
GJI Marine Geosciences and Applied Geophysics

https://doi.org/10.1093/gji/ggac479

Elastic immersive wave experimentation

Xun Li, Johan Robertsson and Dirk-Jan van Manen

ETH Zurich, Institute of Geophysics, Zurich, Switzerland. E-mail: lixunjack@gmail.com

Accepted 2022 November 30. Received 2022 November 29; in original form 2022 September 15

SUMMARY

We describe an elastic wave propagation laboratory that enables a solid object to be artificially immersed within an extended (numerical) environment such that a physical wave propagation experiment carried out in the solid drives the propagation in the extended (numerical) environment and vice versa. The underlying method of elastic immersive wave experimentation for such a laboratory involves deploying arrays of active multicomponent sources at the traction-free surface of the solid (e.g. a cube of granitic rock). These sources are used to accomplish two tasks: (1) cancel outgoing waves and (2) emit ingoing waves representing the first-order interactions between the physical and extended domains, computed using, for example, a finite-difference (FD) method. Higher-order interactions can be built by alternately carrying out the processes for cancelling the outgoing waves and the FD simulations for generating the ingoing waves. We validate the proposed iterative scheme for realizing elastic immersive wave experimentation using 2-D synthetic wave experiments.

Key words: Numerical modelling; Numerical solutions; Body waves; Wave propagation; Wave scattering and diffraction; Wave propagation experiments; Internal absorbing boundaries.

1 INTRODUCTION

Elastic wave experimentation in a laboratory has a number of applications, for instance, for studying material anisotropy (Tsvankin 2012; Qi *et al.* 2015; Yang *et al.* 2016), fracture behaviour characterization (King 2002; Pinto *et al.* 2018; Nosjean *et al.* 2020), experimental time reversal (Derode *et al.* 1995) and noise interferometry (Snieder *et al.* 2002; Hadziioannou *et al.* 2009) and testing wave-based imaging, tomography and inversion methodologies, for example, Marchenko focusing (Wapenaar *et al.* 2014) and full waveform inversion (Tarantola 1984; Brenders & Pratt 2007; Fichtner 2010). Many of these applications would ideally require the experimental domain to be an unbounded solid object, which enables the study of full elastic wavefields, including both compressional (*P*) and shear (*S*) waves (McDonald *et al.* 1983).

However, wave experiments carried out in realistic, size-limited setups typically suffer from unwanted backscattering of waves, including mode-converted reflections, from the traction-free surface enclosing the experimental volume (e.g. Larose *et al.* 2010). These boundary-generated waves often strongly interfere with, or completely mask, the waves of interest, preventing any data interpretation that aims to study the scattering only within the experimental domain (Sivaji *et al.* 2002; Bretaudeau *et al.* 2011; Mikesell & van Wijk 2011; Arthur *et al.* 2012). A conventional solution to this boundary problem relies on increasing the frequency of the probing signals such that the wavelength is orders of magnitude smaller than the size of the experimental domain. This allows separating the imprints associated with the interior scattering from those related to reflecting boundaries in the recorded data. However, the use of frequencies (e.g. 10s to 100s of MHz) that are significantly higher than the seismic band (e.g. 10s to 100s of Hz) is not optimal for studying real Earth materials (with porosity, fluid saturation and fine-scale heterogeneity) for which the physics typically strongly depends on frequency.

An effective solution to remove the boundary problem limited by the use of low frequencies can be anticipated, inspired by so-called acoustic antisound technology, where physical sources actively cancel propagating waves (Williams 1984; Berkhout *et al.* 1993; Cheer 2016). By spanning a physical boundary with arrays of sources, the boundary causing waves to be reflected can be rendered transparent (Becker *et al.* 2020). For a solid experimental domain, Thomsen *et al.* (2019) demonstrated that by using multicomponent piezoelectric sources, elastic waves can be absorbed (including both *P* and *S* modes) at a traction-free end of a 1-D aluminum beam. Hence, as suggested by Thomsen *et al.* (2019), an extension to a 3-D solid object (e.g. a cube of granitic rock) should be possible by deploying arrays of three-component (3C) sources at the free surface of the object.

Fig. 1 illustrates such wave control experimentation. In panel (a), the physical domain bounded by the traction-free surface is shown. Reflections and mode conversions (ray paths 3) of outgoing waves (ray path 1) at the free surface are indicated. In panel (b), an elastic immersive boundary condition (IBC) is applied, complementing the traction-free surface. Outgoing waves (ray path 1) are absorbed at the surface, thereby avoiding unwanted surface-related reflections and mode conversions [i.e. ray paths 3 in panel (a)]. In addition, synthesized waves for the exterior corresponding to scattering from a virtual scatterer are introduced into the

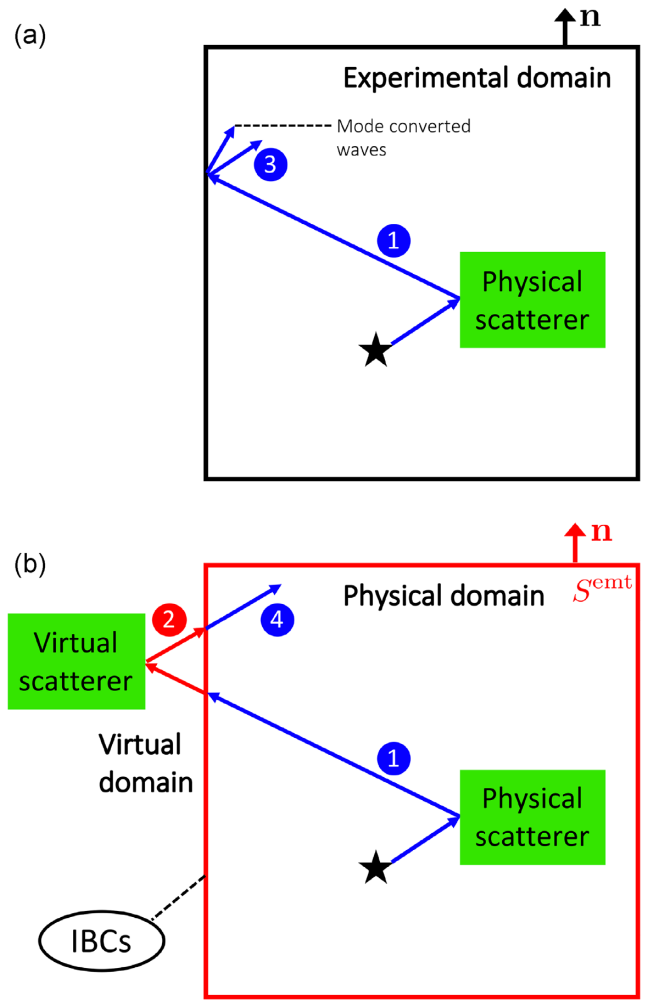

Figure 1. (Colour online) (a) Schematic plot of a physical experiment with a free-surface boundary condition. The solid black square denotes the traction-free surface. The black star denotes an internal source used to generate wave energy. Arrow 1 represents the path of outgoing wave energy, and arrow 3 represents boundary reflections, including mode conversions. (b) Immersive wave experiment. The solid red square denotes the emitting surface S^{emt} enclosing the physical domain. Arrows 2 and 4 represent the paths of wave propagation implicitly outside S^{emt} in a virtual domain and into the physical domain, respectively.

elastic medium through the IBC, creating a new wave state where waves travel back into the physical domain from the exterior (ray path 4). These ingoing waves represent the interaction with the extended (numerical) environment (ray path 2), which involves either an arbitrary medium with numerically modelled waves, or waves that have been recorded experimentally separately (Vasmel *et al.* 2013). In this way, a virtual medium can replace a closed physical reflecting boundary, creating a desired experiment with waves propagating seamlessly between the physical and virtual domains. Following earlier developments for acoustic and 1-D elastic media (Becker *et al.* 2018; Börsing *et al.* 2019; Thomsen *et al.* 2019), we refer to this approach as *elastic immersive wave experimentation*.

Elastic immersive wave experimentation offers a new generation of wave-physics laboratories, with much lower frequencies (1–50 kHz) employed than those used currently to study the elastic properties of solid objects. Also, setting up a virtual domain allows studying media with nonlinearity (e.g. Guyer & Johnson 2009) or unusual metamaterial-like properties such as enhanced absorption, negative constitutive parameters and extremely high anisotropy (e.g. see Pendry 2000; Craster & Guenneau 2012; Wong *et al.* 2017; Park & Lee 2019). A hybrid physical-numerical medium can also reduce the cost of physically making it in a laboratory. The proposed laboratory will enable the experimental study of data-driven focusing methods, such as Marchenko redatuming, by which the response to a virtual source in an unknown medium can be retrieved from the reflection response measured on one side only (Wapenaar *et al.* 2013; Cui *et al.* 2018). One area of broad interest is how to generalize the one-sided scheme to an all-sided scheme to study arbitrarily complex 3-D media. It is not clear that this can be achieved. Progress on this study will increase the understanding of and the ability to harness the multiply scattered wavefield and drive the development of next-generation focusing and imaging techniques used in the laboratory and field.

The key challenge for realizing such immersive experimentation lies in controlling the IBC sources at the boundary of the experimental domain. In previous work on immersive wave experimentation (Vasmel *et al.* 2013; van Manen *et al.* 2007), the time signatures of the IBC sources are calculated by extrapolating the wavefields recorded along a transparent, closed surface *inside* the experimental domain, such that the extrapolation is completed *before* the outward-propagating waves arrive at the boundary (see e.g. Becker *et al.* 2018). Becker *et al.* (2020) implemented such real-time immersive wave experimentation for acoustic wave propagation experiments in a 2-D air-filled waveguide, which enables broad-band interactions (1–10 kHz) with arbitrary exterior virtual environments for physical experiments in it. However for immersing a solid experimental volume, this methodology is not applicable as measuring elastic wavefields at many positions inside the solid is typically not practical due to the inaccessibility of the interior. Therefore, the wavefield recordings have to be made at the same surface as that of the IBC source arrays, effectively ruling out using real-time methods based on wavefield extrapolation for elastic immersive wave experimentation. Instead, the required time signatures for controlling the IBC sources have to be found from free-surface wavefield recordings.

In order to overcome the above-mentioned challenges for realizing elastic immersive wave experimentation, we propose an iterative method that involves alternating physical experiments and numerical, for example, finite-difference (FD) simulations. The iterative scheme combines and improves various existing experimental and numerical modelling methods, including: (1) a wavefield separation method for separating outgoing wavefield constituents based on injection of free-surface recorded data into an FD simulation (Thomsen *et al.* 2021), (2) an internal absorbing boundary condition (IABC) used in the FD simulation to allow the interior of the experimental domain to involve arbitrary unknown media (Li *et al.* 2022b) and (3) a method for computing the interactions between the physical experiment and the virtual environment using a different FD simulation for wavefield extrapolation combined with another IABC. The use of IABCs is critical in each case and thus constitutes a real enabler.

We begin by presenting the theory for elastic IBCs following the derivations by Vasmel *et al.* (2013) for acoustic, and Thomsen *et al.* (2019) for 1-D elastic experiments and describe in detail our iterative method for elastic immersive wave experimentation. In the following section, we show synthetic examples validating the proposed methodology. We then discuss the limitations of our iterative method and highlight further development before summarizing our conclusions.

2 METHOD

2.1 Theory for elastic immersive wave experimentation

Elastic waves propagating in a solid experimental domain can be described through the stress tensor $\tau_{ij}(\mathbf{x}, t)$ and particle velocity $v_i(\mathbf{x}, t)$ governed by the following two coupled first-order differential equations (Virieux 1986):

$$\rho(\mathbf{x})\frac{\partial v_i(\mathbf{x}, t)}{\partial t} = \frac{\partial \tau_{ij}(\mathbf{x}, t)}{\partial x_j} + f_i(\mathbf{x}, t) \tag{1}$$

and

$$\frac{\partial \tau_{ij}(\mathbf{x}, t)}{\partial t} = c_{ijkl}(\mathbf{x})\frac{\partial v_l(\mathbf{x}, t)}{\partial x_k} + c_{ijkl}(\mathbf{x})h_{kl}(\mathbf{x}, t), \tag{2}$$

where $\mathbf{x}$ represents a Cartesian coordinate, t is time, $v_i(\mathbf{x}, t)$ represents the particle velocity wavefield (with spatial direction x_i), $\tau_{ij}(\mathbf{x}, t)$ represents the stress tensorial wavefield (with components ij), $\rho(\mathbf{x})$ is the mass density, c_{ijkl} is the fourth-rank stiffness tensor, f_i corresponds to a distribution of body force density sources and h_{kl} corresponds to a distribution of deformation rate density sources. Einstein's summation convention applies to repeated subscripts.

Betti's reciprocity theorem (Aki & Richards 2002) can be derived from eqs (1) and (2) (see Appendix A), and through this theorem, the particle velocity wavefield v_n^{full} in the physical domain of an immersive wave experiment [Fig. 1(b)] can be expressed as

$$v_n^{\text{full}}(\mathbf{x}, t) = \int G_{n,i}^{v,f}(\mathbf{x}, t \mid \mathbf{x}_s, 0) * f_i^{\text{full}}(\mathbf{x}_s, t)\, \mathrm{d}V(\mathbf{x}_s) + \oint_{S^{\text{emt}}} G_{n,i}^{v,f}(\mathbf{x}, t \mid \mathbf{x}_{\text{emt}}, 0) * \tau_{ij}^{\text{full}}(\mathbf{x}_{\text{emt}}, t) n_j\, \mathrm{d}S(\mathbf{x}_{\text{emt}}), \tag{3}$$

where S^{emt} is the emitting surface, n_j denotes the normal vector component of S^{emt}, the symbol $*$ denotes temporal convolution, $\mathbf{x}_s$ is the location(s) of source(s) inside S^{emt}, f_i^{full} denotes a distribution of body force sources, $\tau_{ij}^{\text{full}}(\mathbf{x}_{\text{emt}}, t)\, n_j$ represents normal tractions at the locations of S^{emt} in the full domain, combining the physical experiment and virtual environment, the Green's function $G_{n,i}^{v,f}(\mathbf{x}, t \mid \mathbf{x}_{\text{emt}}, 0)$ represents the particle velocity (superscript v) in the n direction (subscript n) recorded at the location $\mathbf{x}$ due to an impulsive point source of body force (f) in the i direction (subscript i) and $G_{n,i}^{v,f}(\mathbf{x}, t \mid \mathbf{x}_s, 0)$ denotes the impulse response due to an interior source at $\mathbf{x}_s$. These Green's functions involve multiple components for the source and receiver fields and are associated with the medium inside the physical experimental domain.

For a physical wave experiment that is only associated with a distribution of interior sources, that is, without exciting any active sources placed on the emitting surface S^{emt}, the wavefield in the interior can be expressed as

$$v_n^{\text{phy}}(\mathbf{x}, t) = \int G_{n,i}^{v,f}(\mathbf{x}, t \mid \mathbf{x}_s, 0) * f_i^{\text{phy}}(\mathbf{x}_s, t)\, \mathrm{d}V(\mathbf{x}_s). \tag{4}$$

The derivation of eq. (4) can also be found in Appendix A. When comparing eqs (3) and (4) and provided that the distribution of interior sources inside V is equal (i.e. $f_i^{\text{full}} = f_i^{\text{phy}}$), the following relation holds:

$$v_n^{\text{full}}(\mathbf{x}, t) = v_n^{\text{phy}}(\mathbf{x}, t) + \oint_{S^{\text{emt}}} G_{n,i}^{v,f}(\mathbf{x}, t \mid \mathbf{x}_{\text{emt}}, 0) * \tau_{ij}^{\text{full}}(\mathbf{x}_{\text{emt}}, t) n_j\, \mathrm{d}S(\mathbf{x}). \tag{5}$$

Hence, the difference between the particle velocity wavefields in the extended, full domain and the truncated, physical domain is equal to the integral over the emitting surface S^{emt} of the temporal convolution between the Green's functions associated with the truncated, physical domain and the normal tractions $\tau_{ij}^{\text{full}} n_j$ measured in the full, immersive domain. Hence, the surface integral on the right-hand side of eq. (5) provides the effect of elastic immersive wave

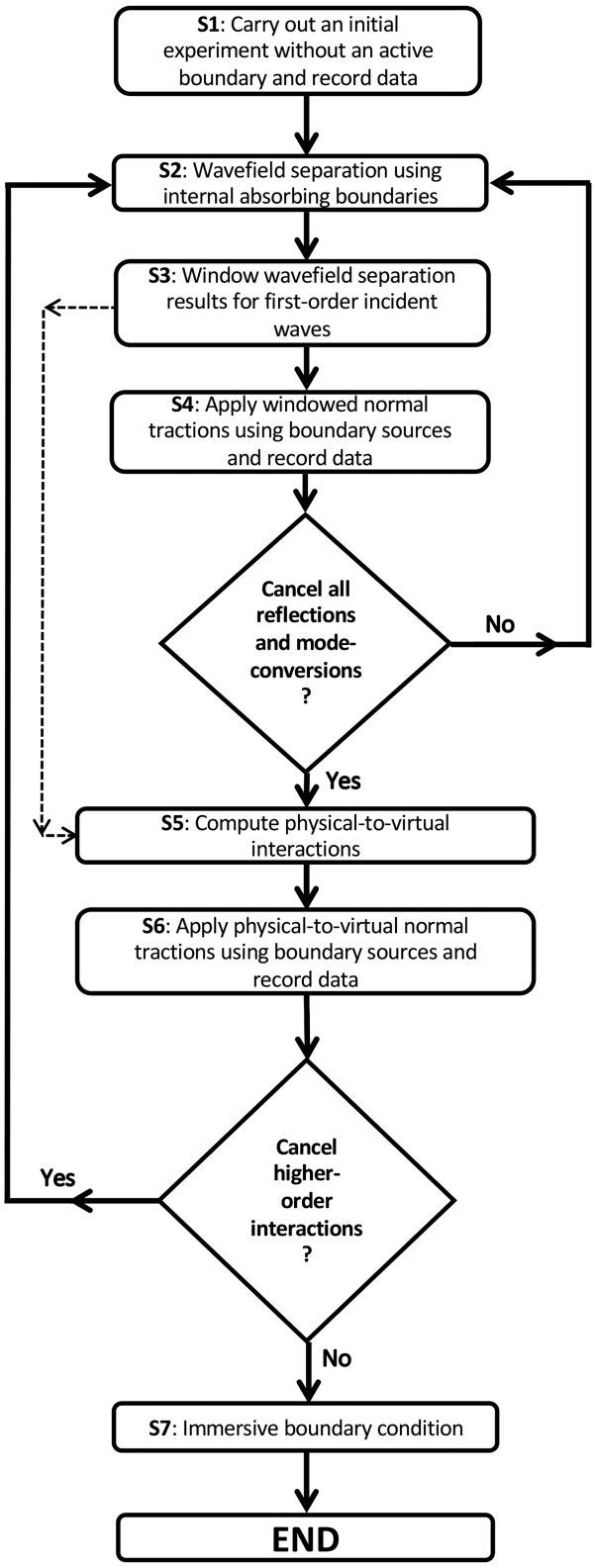

Figure 2. Flowchart describing the iterative method for elastic immersive wave experimentation.

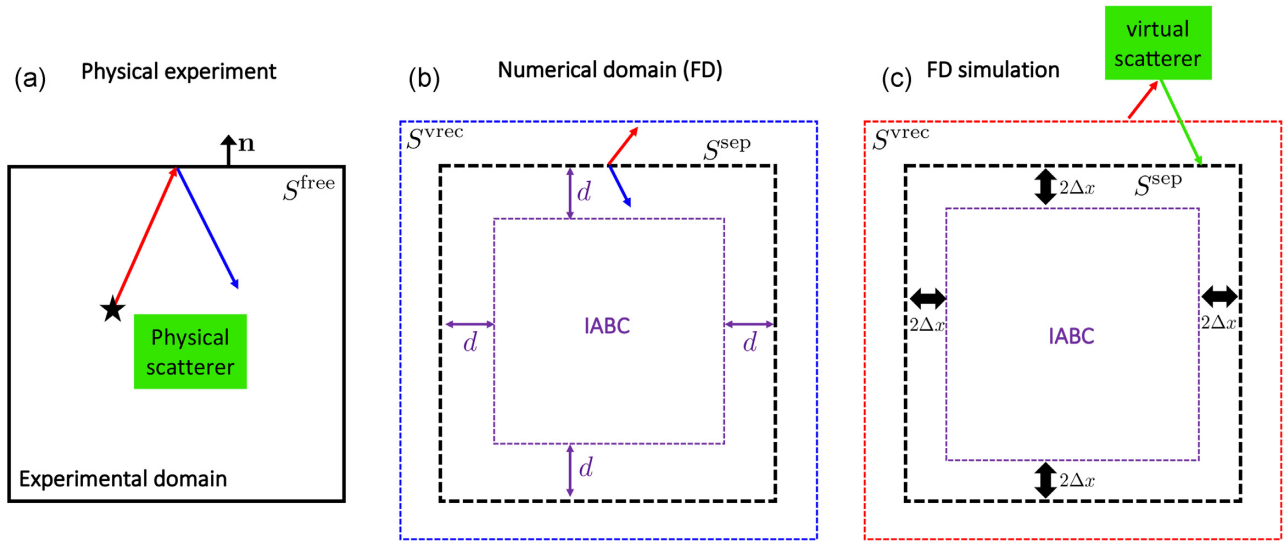

Figure 3. (Colour online) 2-D schematic plots of (a) a physical experiment (Step 1 in Fig. 2), (b) the wavefield separation carried out in an FD simulation (Step 2) and (c) computing the physical-to-virtual interaction in a separate FD simulation (Step 5). (a) The solid black square denotes the free surface S^{free} enclosing the physical experiment. (b) The dashed black square denotes the wavefield injection surface S^{sep}. The dashed purple square denotes the IABC region. The dashed blue square denotes the virtual recording surface S^{vrec}. (c) The dashed red square denotes the surface S^{vrec} on which the elastic wavefields obtained at S^{vrec} in panel (b) are injected for wavefield extrapolation. The dashed black square denotes the surface S^{sep} for wavefield recording. (a)–(c) The red arrow denotes (separated) outgoing wave energy, while the blue arrow denotes (separated) ingoing wave energy. The green arrow denotes the (ingoing) wave energy scattered by the virtual medium.

experimentation, namely:

$$v_n^{\text{emt}}(\mathbf{x}, t) = \oint_{S^{\text{emt}}} G_{n,i}^{v,f}(\mathbf{x}, t \mid \mathbf{x}_{\text{emt}}, 0) * \tau_{ij}(\mathbf{x}_{\text{emt}}, t)\, n_j \, \mathrm{d}S(\mathbf{x}_{\text{emt}}), \quad (6)$$

where $v_n^{\text{emt}}(\mathbf{x}, t)$ represents the particle velocity wavefield inside the experimental domain due to the densely spaced distribution of sources on the emitting surface S^{emt} (also the boundary of the experimental domain). The convolution term $G_{n,i}^{v,f} * \tau_{ij}\, n_j$ shows that the immersive effect inside the experimental domain is provided by a dense array of body force sources f_i (on S^{emt}) with normal tractions $\tau_{ij}\, n_j$ as the source signatures (Li *et al.* 2022a). However, note that these normal tractions are the tractions in an ideal immersive experiment where the free surface of a physical experiment has been perfectly replaced by a transparent boundary and the surrounding virtual medium [Fig. 1(b)]. Hence, to establish an immersive field for the desired physical experiment, the active boundary condition depends on the desired field itself. Note that a similar situation exists in acoustic immersive wave experimentation (Becker *et al.* 2020), but for the elastic case, one cannot obtain the desired fields (normal tractions) by extrapolating the wavefields from the interior as it is typically impossible to measure the wavefields inside a solid.

The entire challenge of immersing an elastic experiment into a virtual, numerical environment can be divided into two independent tasks: (1) cancel reflections of outgoing waves at the boundaries of an experimental domain and (2) generate waves at the boundaries representing the (first-order) interactions between the physical outgoing waves and a virtual medium. As we will see below, Tasks (1) and (2) must be *iterated* to correctly include higher than first-order interactions. According to this principle, we partition the required normal tractions $\tau_{ij}(\mathbf{x}_{\text{emt}}, t)\, n_j$ needed for immersive wave experimentation as

$$\tau_{ij}^{\text{full}}(\mathbf{x}_{\text{emt}}, t) n_j = \tau_{ij}^{\text{inc}}(\mathbf{x}_{\text{emt}}, t) n_j + \tau_{ij}^{\text{vir}}(\mathbf{x}_{\text{emt}}, t) n_j + \tau_{ij}^{\text{hig}}(\mathbf{x}_{\text{emt}}, t) n_j \quad (7)$$

where $\tau_{ij}^{\text{inc}}\, n_j$ and $\tau_{ij}^{\text{vir}}\, n_j$ are the normal tractions corresponding to Tasks (1) and (2), respectively, and $\tau_{ij}^{\text{hig}}\, n_j$ corresponds to the higher-order interactions between the physical experiment and virtual environment.

The incident part of the normal tractions $\tau_{ij}^{\text{inc}}\, n_j$, corresponding to physical primary[1] outgoing waves [ray path 1 in Fig. 1(a)] have to be sought from data recorded at the free surface, which are the three components of the particle velocity vector wavefield $\mathbf{v}^{\text{free}}(\mathbf{x}_{\text{rec}}, t)$. This requires separating the free-surface data, which is achieved using an FD propagator as described below.

The normal tractions $\tau_{ij}^{\text{vir}}\, n_j$ (in eq. 7) are needed for generating the ingoing wave energy at the free surface. Obtaining the tractions $\tau_{ij}^{\text{vir}}\, n_j$ involves extrapolating the separated outgoing waves to make them interact with a numerical virtual environment (described below). The normal tractions $\tau_{ij}^{\text{hig}}\, n_j$ correspond to higher-order interactions between the physical experiment and its surrounding virtual domain. These higher-order interactions can be obtained by repeatedly applying the approaches for incident wavefield separation and extrapolation through the virtual medium. This iterative strategy can be understood by comparing it to acoustic IBCs (Becker *et al.* 2020): in an acoustic immersive experiment, higher-order interactions are included in a real-time *recursive* implementation, while in an elastic experiment, we have to, in principle, carry out an iterative method manually by alternating physical experiments, incident wavefield separation, and extrapolation for fulfilling the goal of immersing an elastic wave experiment into a virtual medium.

[1]As will be explained in detail below, only primary outgoing waves, that is, the incident part of first-order interactions with the free surface, must be considered since higher-order interactions with the free surface will no longer exist once the first-order interactions have been cancelled.

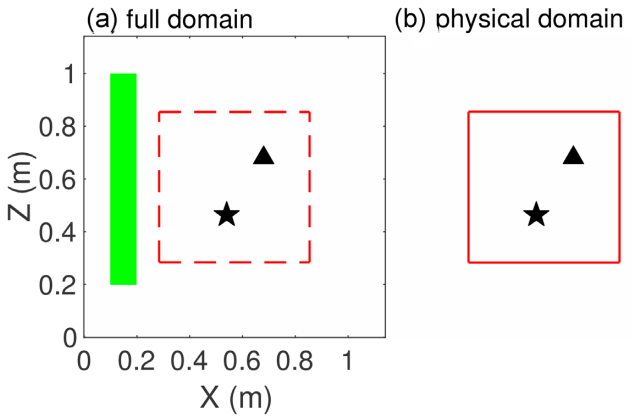

Figure 4. (Colour online) Model used for synthetic immersive wave experiments. (a) Full model including the virtual and physical domains whose interface is denoted by the dashed red square. The black star denotes a source that generates wave energy, and the black triangle denotes a receiver. The green block denotes the density scatterer placed in the virtual domain. (b) Immersive wave experiment bounded by the emitting surface S^{emt} (solid red square).

2.2 An iterative method for elastic immersive wave experimentation

Fig. 2 shows a flowchart describing an iterative method for elastic immersive wave experimentation. This iterative scheme involves two cycles of steps. Steps 2–4, comprising the inner cycle ('S' for 'Step' in Fig. 2), implement the calculation and application of the normal tractions $\tau_{ij}^{\mathrm{inc}}\, n_j$ (cf. eq. 7) for the purpose of cancelling primary outgoing waves in the physical experiment, whereas Steps 5 and 6 implement the computation and application of the normal tractions $\tau_{ij}^{\mathrm{vir}}\, n_j$ for producing first-order virtual-to-physical ingoing waves. The outer cycle, comprising Steps 5 and 6 and the inner cycle (Steps 2 to 4), is subsequently repeated to compute and include higher-order interactions (i.e. $\tau_{ij}^{\mathrm{hig}}\, n_j$), eventually creating the full elastic immersive wave experiment. In the following, we discuss the iterative method step by step and introduce various experimental and numerical methodologies.

2.2.1 S1: carry out an initial experiment without an active boundary and record data

The first step comprises recording particle velocity data $v_i^{\mathrm{free}}(\mathbf{x}_{\mathrm{rec}}, t)$ at the free surface bounding a solid experimental volume. The data are associated with one or more sources in the interior of the experimental domain and should be recorded at the free surface when the IBC sources on the same surface are *not* active [Fig. 3(a)].

2.2.2 S2: wavefield separation using internal absorbing boundaries

The second step is based on the wavefield separation method proposed by Li *et al.* (2022b), which involves injecting the free-surface data into a time-domain FD simulation. This wavefield injection, together with internal absorbing boundaries incorporated into the FD simulation, allows separating the incident part of the data without any knowledge of the medium properties in the interior of the physical experimental domain.

To achieve the wavefield separation, deformation rate tensor sources are first computed from the recorded particle velocity data and subsequently used as a source term in eq. (2) when solving eqs (1) and (2) alternately (see Li *et al.* 2022b, for details). In this paper, we employ an FD scheme that is second-order accurate in both time and space. Note that the wavefield injection surface S^{sep} must have the same geometry as the free surface S^{free} enclosing the experimental domain, including the same normal $\mathbf{n}$. For this wavefield injection, the only requirement is knowledge of the correct model parameters (i.e. c_{ijkl}, ρ) at the injection locations ($\mathbf{x}_{\mathrm{sep}}$ on S^{sep}), matching the physical parameters at the recording locations ($\mathbf{x}_{\mathrm{rec}}$ on S^{free}) in the physical experiment.[2] The elastic parameters in other parts of the FD model can be set to equal the parameters of the background medium as measured or estimated from the physical experimental domain.

Fig. 3(b) shows the geometry of the wavefield separation for which the data injection on the surface S^{sep} radiates the outgoing wavefield constituents of the data outward of S^{sep} and the ingoing constituents inward of S^{sep}. In the FD simulation, we deploy a novel IABC inside the wavefield injection surface S^{sep} (for details, see Li *et al.* 2022b). Around the FD domain, a radiation boundary condition is implemented with convolutional perfectly matched layers to absorb the separated, outgoing waves propagating out from the FD domain.

The reconstructed ingoing waves inside the wavefield injection surface S^{sep} are by-products of the wavefield separation and not needed. The ingoing waves are annihilated by the IABC in order not to interfere with the isolation of the outgoing part of second- and higher-order free-surface interactions. The IABC for wavefield separation involves a parameter d, which defines the distance between the injection surface S^{sep} and the IABC boundary in the FD simulation. In Li *et al.* (2022b), this parameter d was set to be two FD gridpoints (the minimum allowed value) such that the incident parts of all free-surface interactions are obtained correctly. However for elastic immersive wave experimentation, only the first-order incident wavefield, that is, normal traction quantities $\tau_{ij}^{\mathrm{inc}}\, n_j$, are needed to cancel *all* outgoing waves in the physical experiment.

An, in principle, straightforward solution to obtain only the first-order incident waves would be to isolate them from the separated wavefield using a windowing approach. However, in practice, when the distance d in the FD simulation is chosen as the minimal value (two FD gridpoints), second-order incident waves immediately follow first-order incident waves near the corners of the wavefield injection surface S^{sep}. This causes difficulty in isolating the desired first-order waves there. To circumvent this problem, we place the IABC further away from the injection surface S^{sep}, which allows some of the ingoing waves to travel across the interior near the corners of the domain. Provided that the model is correct in the corners, these ingoing waves will destructively interfere with the wavefield injection itself, preventing the separation of the second-order outgoing waves near the corners and guaranteeing a minimum time separation between first- and second-order outgoing waves. Note that this implies a requirement that unknown scatterers exist only deep inside the solid (i.e. at depth $>d$). This is further discussed in Section 4.

[2] A solid experimental domain usually involves constant elastic parameters near its free surface but when the elastic parameters at the near surface vary, one needs to interpolate on the model away from the injection locations such that the model smoothly changes from the laterally varying near surface to a constant interior. This ensures that no artificial backscattering can occur near the injection surface.

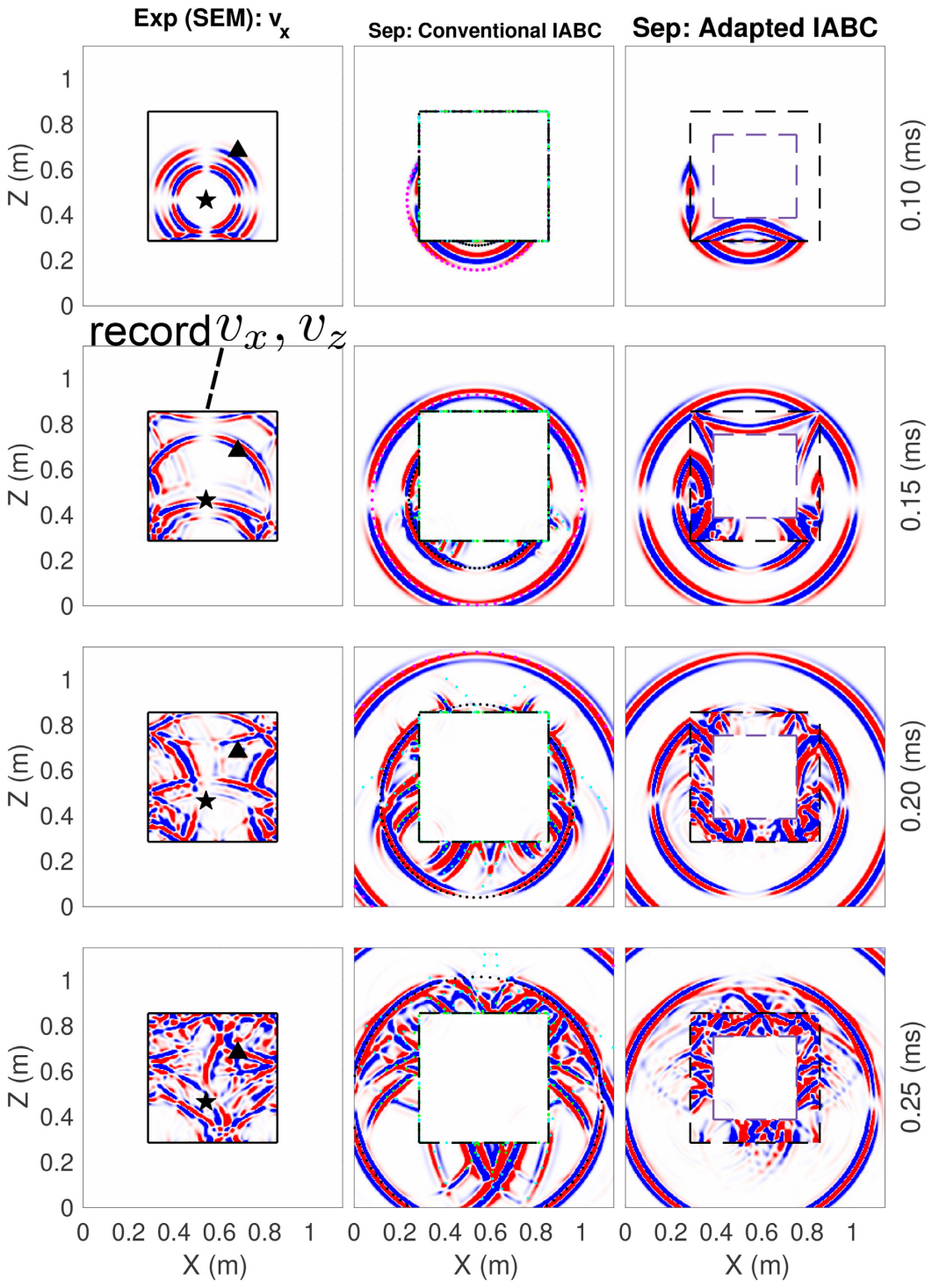

Figure 5. (Colour online) Snapshots of the 2-D synthetic wave experiment and the associated wavefield separations. The first column shows the particle velocity wavefield v_x in the wave experiment at different simulation times. The solid black square denotes the free-surface boundary of the experimental domain, and the black star and triangle denote the interior source and receiver, respectively. The second column shows the FD simulation (τ_{xx} wavefield) for the wavefield separation together with the conventional IABC used. The dashed black square denotes the wavefield injection surface S^{sep}. The magenta dots overlaying the wavefield denote the wave front of the primary outgoing *P* wave (*p*), while the cyan dots denote the secondary *P* waves (including *pp* and *sp*). The black dots denote the wave front of the primary outgoing *S* wave (*s*), while the green dots denote the secondary *S* waves (including *ss* and *ps*). The third column shows the FD simulation with the adapted IABC applied. The dashed purple square denotes the internal absorbing boundary.

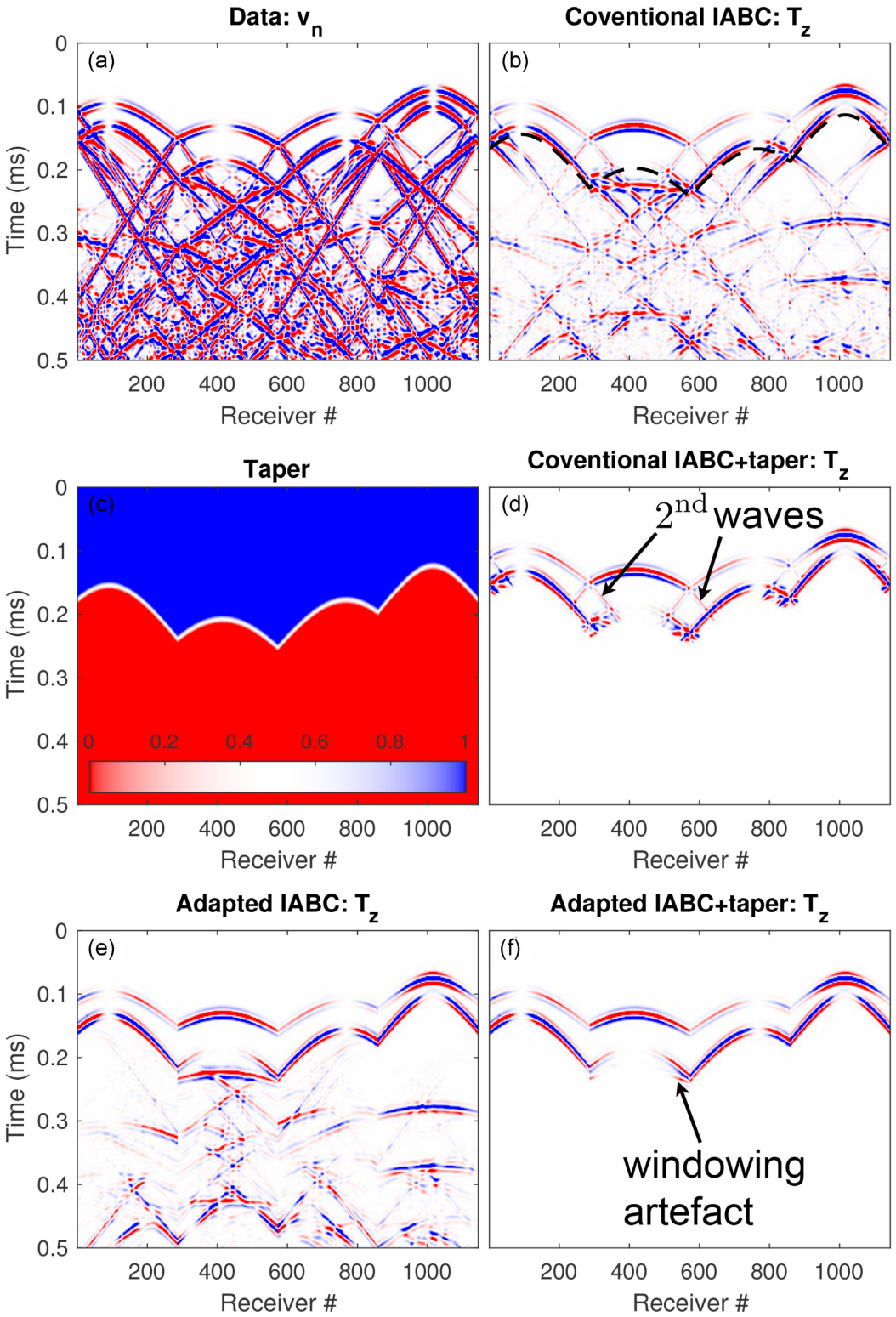

Figure 6. (Colour online) (a) Recorded v_n data (normal particle velocities) at the free surface of the physical experiment. The receivers along the free surface are counted clockwise from the top, left corner of the surface S^{free} in Fig. 4. (b) Normal component of the normal traction vector T_z retrieved from the FD simulation, with the conventional IABC method used. The dashed black line delineates the end times of the windows selected (the start time is $t = 0$). (c) Taper made from the time windows annotated in panel (b). (d) Windowed normal traction vector T_z [from panel(b)] applied to the sources at the free surface. (e) T_z retrieved from the FD simulation, with the adapted IABC method used. (f) Windowed T_z [from panel(e)] applied to the sources at the free surface.

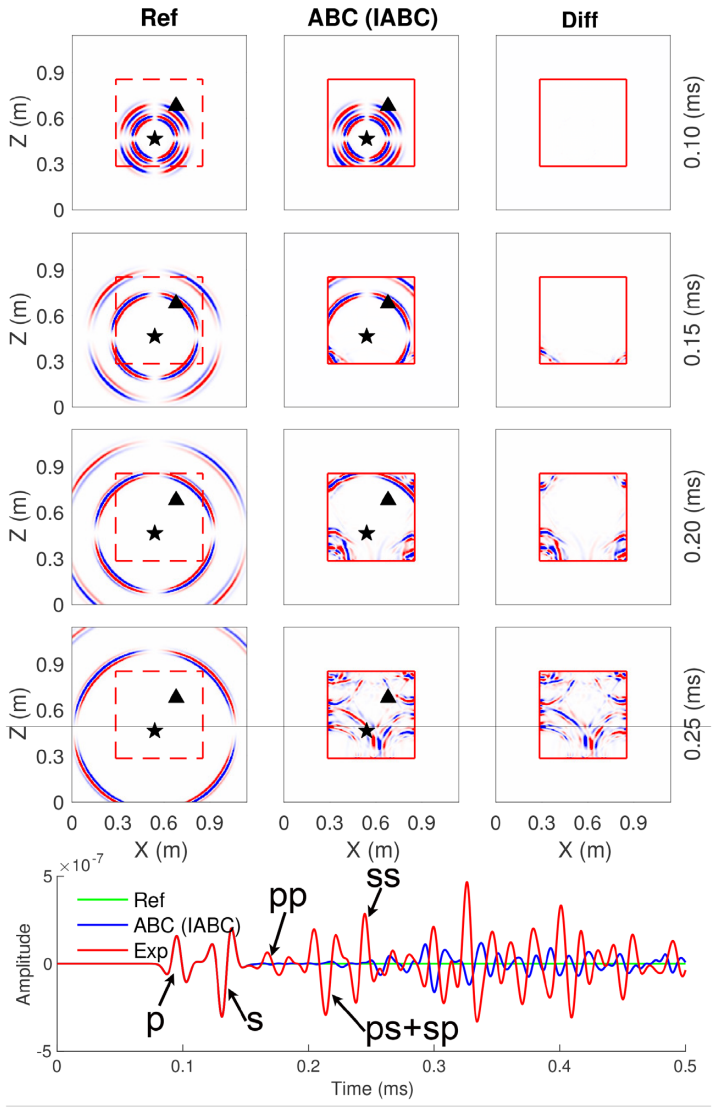

Figure 7. (Colour online) Synthetic wave experiment with the normal tractions obtained using both the conventional IABC method and windowing approach. The first column shows the snapshots of the reference simulation (v_x wavefield), and the second column shows the wave experiment. The third column shows the difference between the synthetic (second column) and reference (first column) simulations inside the emitting surface S^{emt} (red square). Otherwise, key as in Fig. 5. The trace plot shows the recorded v_x signals at the receiver (black triangle) placed in the reference experiment ('Ref'), synthetic experiment ('ABC'), and the experiment without the active boundary ('Exp').

From the FD simulation for wavefield separation only the outgoing normal traction quantities are needed for cancelling the reflections and mode conversions at the free surface of the physical experiment. As illustrated in Appendix B, these tractions can be recorded exactly at the locations of the injection surface S^{sep}. Lastly, in anticipation of the extrapolation of the outgoing waves through the virtual domain (to be described in Section 2.2.5), full elastic wavefields are recorded in the FD simulation at a virtual recording surface S^{vrec} placed two FD gridpoints away from the wavefield injection surface S^{sep} [see Fig. 3(b)].

2.2.3 S3: window wavefield separation results for first-order incident waves

The separated outgoing waves in Step 2 contain higher-order interactions with the free surface, which are undesired for cancelling outgoing waves since they correspond to already cancelled reflections and mode conversions. Enabled by the use of a larger d (in IABC) in the previous step, a simple windowing approach is used to isolate the first-order incident components.

This windowing approach is straightforward when primary waves can be separated from higher-order waves based on their arrival times. If this is not the case, the windowing has to be implemented conservatively to ensure the absence of second- or higher-order free-surface interactions. For example, if second-order incident P waves arrive before first-order incident S waves, then the use of too long windows could give rise to artefacts as previously cancelled waves are re-radiated into the experimental volume. This rule of selecting windows is critical to the convergence of the iterative method, as the incorrect inclusion of higher-order waves will lead to erroneous, superfluous boundary wavefield generation in the next step. This erroneous wavefield, if it is generated, may not be further cancelled in the later iterations.

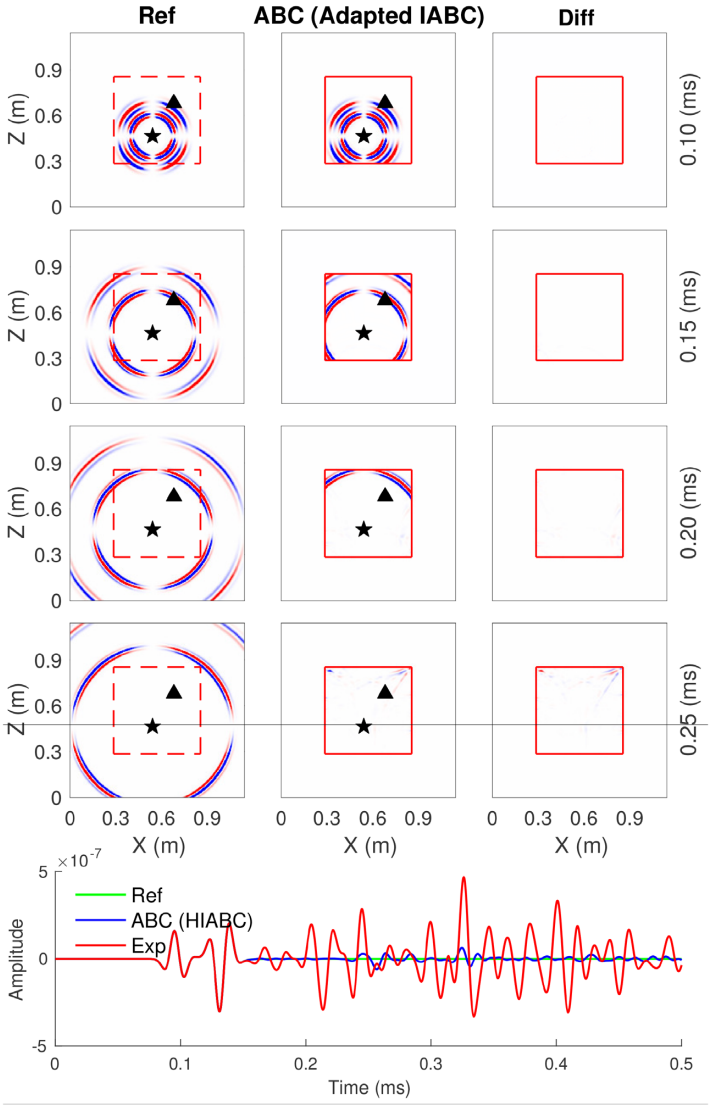

Figure 8. (Colour online) Synthetic absorbing wave experiment with the source signatures calculated using the adapted IABC method and windowing approach [Fig. 6(f)].

2.2.4 S4: apply windowed normal tractions using boundary sources and record data

Applying the separated, windowed normal traction components as the signatures of the active boundary sources in a new physical experiment, together with the original (distribution of) source(s) in the interior, achieves the desired effect of absorbing (a part of) the first-order outward-propagating waves from the interior of the experimental domain, preventing their reflections and mode conversions at the free surface. During this new physical experiment, data are once again recorded at the 'free' surface. Recall that in Step 1 (Section 2.2.1), no boundary sources were active, and data can be recorded at all times. But in this and later steps of the inner iteration (Fig. 2), no data should be recorded when the boundary sources are active as incident waves that have been cancelled in earlier iterations should not be 'recorded' again in the current iteration.

In the inner cycle of the proposed scheme (Fig. 2), Steps 2–4 are iterated to gradually cancel any first-order outgoing waves that have not been cancelled in the earlier rounds. This strategy exploits the fact that cancelling first-order waves also removes their associated second- and higher-order multiples that may overlap with the later-arriving first-order outgoing waves. In doing so, we iteratively build up a physical absorbing boundary condition (ABC) for the wave experiment, first accounting for all first-order incident waves (i.e. $\tau_{ij}^{\mathrm{inc}}\, n_j$) and eventually in subsequent iterations, absorbing all outgoing waves including their free-surface related reflections and mode conversions.

In the following, we will refer to first-order outgoing waves as primary outgoing waves in order to avoid confusion between the order of the free-surface interactions and the order of the physical-to-virtual interactions.

2.2.5 S5: compute physical-to-virtual interactions

After cancelling all unwanted reflected waves at the physical surface, the same set of boundary sources should further generate the first-order interactions of the primary outgoing waves and the virtual medium, through the time signatures $\tau_{ij}^{\mathrm{vir}}\, n_j$ (see eq. 7). For this purpose, we extrapolate the recorded outgoing full elastic wavefield into a separate FD simulation such that it can interact with a desired, virtual environment, as shown in Fig. 3(c). We employ a method of

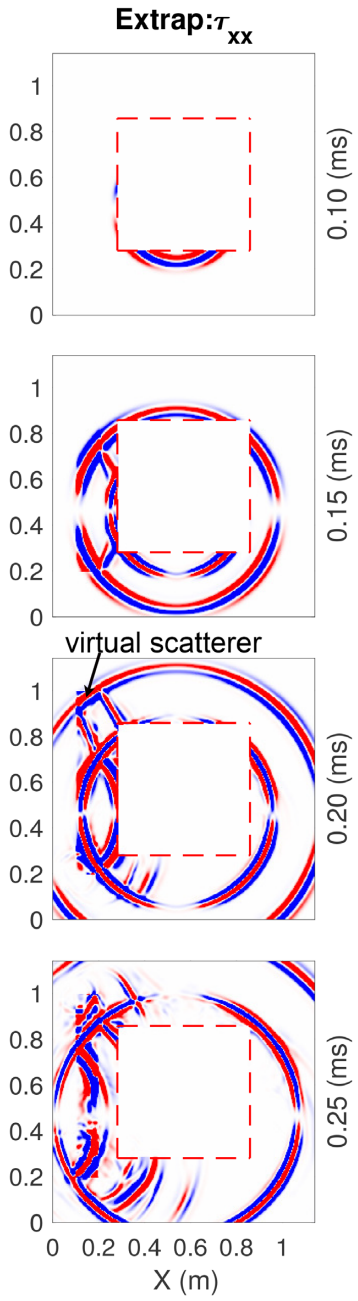

Figure 9. (Colour online) Snapshots of the wavefield extrapolation. The dashed red square denotes the surface S^{vrec}. Otherwise key as in Fig. 5.

multiple point sources (MPS) to implement the wavefield recording and injection involved in the separate FD simulation (Li *et al.* 2022a).

For this wavefield extrapolation, we use the full elastic wavefields first obtained at the virtual recording surface S^{vrec} [Step 2 in Figs 2 and 3(b)] and then windowed accordingly, using the same approach as in Step 3. Through the inner cycle of the iteration (Steps 2–4), the windowed elastic wavefields are accumulated as total separated, primary outgoing waves (the dashed connection in Fig. 2). These total elastic wavefield quantities are injected into an FD simulation along a transparent surface that has the same geometry as the virtual recording surface S^{vrec} [Fig. 3(c)]. The goal of this numerical wavefield injection is to isolate the primary, outgoing waves outside the surface S^{vrec} (different from the wavefield injection used for wavefield separation in Step 2). This allows the waves to interact with the virtual environment defined outside the surface S^{vrec} in the FD simulation. The model parameters inside the virtual recording surface S^{vrec} are set to be the background model parameters for the experimental domain, and an IABC is incorporated inside the surface S^{sep} such that the backscattered virtual waves cannot travel through the region enclosed by the surface S^{sep}. Note that this IABC should be as close as numerically feasible to the surface S^{sep} with $d = 2\Delta x$ where Δx is the size of an FD gridpoint. In this FD simulation for extrapolating the elastic wavefields, the desired virtual-to-physical interactions are obtained at the surface S^{sep} (note that no wavefield injection is made at this surface). Only the normal tractions $\tau_{ij}^{\text{vir}} n_j$ need to be recorded at the surface S^{sep} to reproduce these waves at the free surface of the physical experiment.

2.2.6 S6: apply physical-to-virtual normal tractions using boundary sources and record data

Applying the normal tractions $\tau_{ij}^{\text{vir}} n_j$ obtained in Step 5 [Fig. 3(c)] to the active source boundary generates the first-order interaction between the physical experiment and virtual domain. The source signatures, which have already included the incident tractions $\tau_{ij}^{\text{inc}} n_j$ (obtained in Step 4), are further complemented by the normal tractions $\tau_{ij}^{\text{vir}} n_j$ (eq. 7), and used to drive the active boundary sources in the physical experiment.

Then wavefield recording is carried out while physically generating the ingoing physical-to-virtual waves as these waves eventually become outgoing again and should then in turn be cancelled at the free surface. For this purpose, the new outgoing waves have to be recorded when they arrive *again* at the free surface, for wavefield separation (Step 2) in the next iteration (Fig. 2). Note that different from Step 4, the recording is carried out *simultaneously* and *collocated* with the generation of the ingoing waves at the free surface. Since the ingoing wavefield constituents are completely known through the virtual medium, the subsequent wavefield separation should proceed by removing the known imprints in the data that are related to the *production* of ingoing waves at the same recording locations.

2.2.7 S7: immersive boundary condition

Carrying out Step 1 and iterating Steps 2–4, followed by Steps 5 and 6 (Fig. 2), achieve both the cancellation of reflections and mode conversions at the free surface and the production of desired first-order interactions with the virtual exterior at the free surface of a physical experiment. However, a full elastic IBC still needs to account for the higher-order interactions between the physical and virtual domains.

We do this by first re-iterating Steps 2–4 to cancel the newly emerged outgoing waves at the free surface in the wave experiment (with the data recorded in Step 6). Then one can go through Step 5 again, extrapolating the new physical outgoing waves into the numerical virtual environment, and Step 6, generating the second-order interaction between the physical experiment and virtual medium. For even higher-order interactions between the physical and virtual domains, one can repeat the two cycles of steps as shown in Fig. 2, until all orders of interactions are accounted for within the time of the physical experiment. This allows to obtain the normal tractions $\tau_{ij}^{\text{hig}} n_j$, and summing up all the normal tractions sought for eq. (7) forms a complete method of elastic immersive wave experimentation.

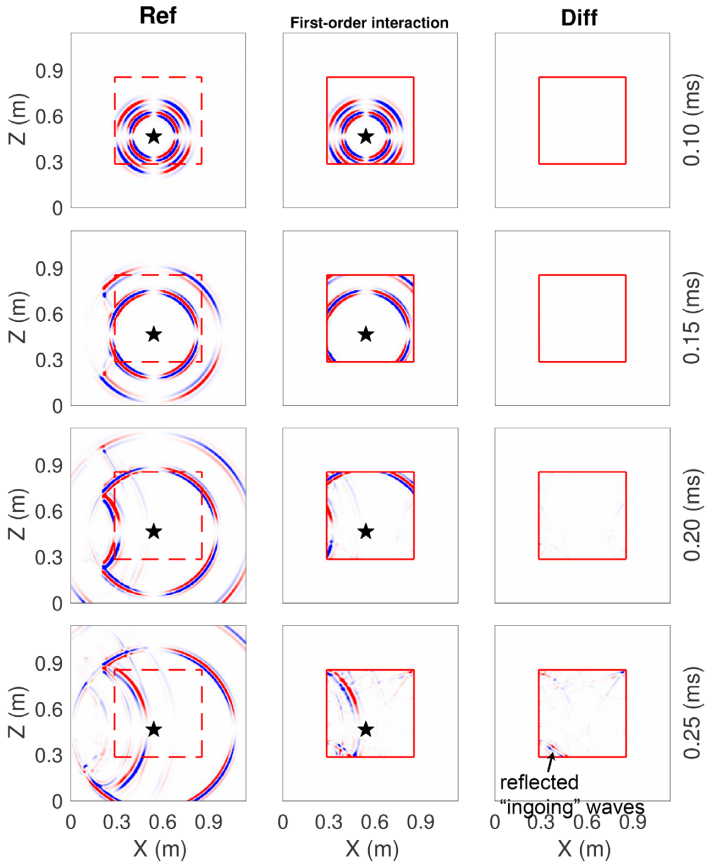

Figure 10. (Colour online) Wave experiment with the first-order physical-to-virtual interaction generated. Key as in Fig. 8.

3 RESULTS

3.1 Model

In this section, we describe a 2-D synthetic elastic wave experiment, illustrated in Fig. 4. Note that our iterative method is designed for 3-D experiments, and showing 2-D synthetic examples is only for the purpose of illustration. We assume an isotropic medium in the physical wave experiment [Fig. 4(b)], which allows the stiffness tensor c_{ijkl} in eq. (2) to be replaced by Lamé parameters λ and μ via the relation $c_{ijkl}(\mathbf{x}) = \lambda(\mathbf{x})\delta_{ij}\delta_{kl} + \mu(\mathbf{x})(\delta_{ik}\delta_{jl} + \delta_{jk}\delta_{il})$ where δ is the Kronecker delta. The parameters λ and μ are related to the compressional and shear wave velocities V_P and V_S via $\lambda = \rho(\mathbf{x})[V_P^2(\mathbf{x}) - 2 \cdot V_S^2(\mathbf{x})]$ and $\mu = \rho(\mathbf{x})V_S^2(\mathbf{x})$. The compressional wave velocity is set to $V_P = 4000\ \mathrm{m\,s^{-1}}$, the shear wave velocity is $V_S = 2500\ \mathrm{m\,s^{-1}}$ and the mass density is $\rho_0 = 2600\ \mathrm{kg\,m^{-3}}$. The length x and height z of the physical domain are both 0.57 m. A body force source f_z pointing upwards is placed inside the physical domain at $(x_{\mathrm{src}}, z_{\mathrm{src}}) = (0.255, 0.18)$ m. The source signature corresponds to a Ricker wavelet with peak frequency $f_p = 50$ kHz. The virtual domain connecting to the physical experiment contains a strongly scattering heterogeneity of density $6\rho_0$ while the compressional and shear velocities are homogeneous across the physical and virtual domains. The modelled experimental duration is 0.5 ms.

Synthetic wave experiments resembling the physical experiments are simulated with spectral-element modelling (SEM) software SALVUS (Afanasiev *et al.* 2018). The number of elements used in the SEM simulation (along both x- and z-directions) across the experimental domain is 57, while the Gauss–Lobatto–Legendre (GLL) order of each element is 4. The time step of the SEM simulation is chosen to satisfy the CFL (Courant–Friedrichs–Lewy) criterion (Igel 2017).

3.2 Cancelling first-order incident waves

First, we show how Steps 1–4 (in Fig. 2) are sequentially carried out to achieve a physical ABC, preventing reflections and mode conversions of waves incident on the free surface from the interior. The first column of Fig. 5 shows snapshots during the 'acquisition' of the initial data (without IBCs), which are particle velocities v_x and v_z obtained across the free surface bounding the physical experiment (Step 1 in Fig. 2). Fig. 6(a) shows the data recorded at the free surface, which are dominated by multiples of the primary incident wavefields.

For the wavefield separation (Step 2 in Fig. 2), the recorded free-surface data (v_x and v_z) are injected into a larger FD simulation over a fully homogeneous model which has a length and height of 1.14 m. The wavefield injection surface S^{sep} is placed in the middle of the FD model, which has the same (background) model parameters as those at the recording locations of the physical experimental volume. The FD grid size is set to be 25 gridpoints per average S wavelength ($\frac{1}{25}V_s/f_p$), satisfying a rule of thumb (>20) in FD modelling (Igel 2017).

Before proceeding with the proposed IABC method in Step 2 (Fig. 2), we first demonstrate the issue of using a 'conventional' IABC methodology (with d equal to only two FD gridpoints) in the second column of Fig. 5. As expected, very little energy is present inside the injection surface S^{sep}. Superimposed on the separated

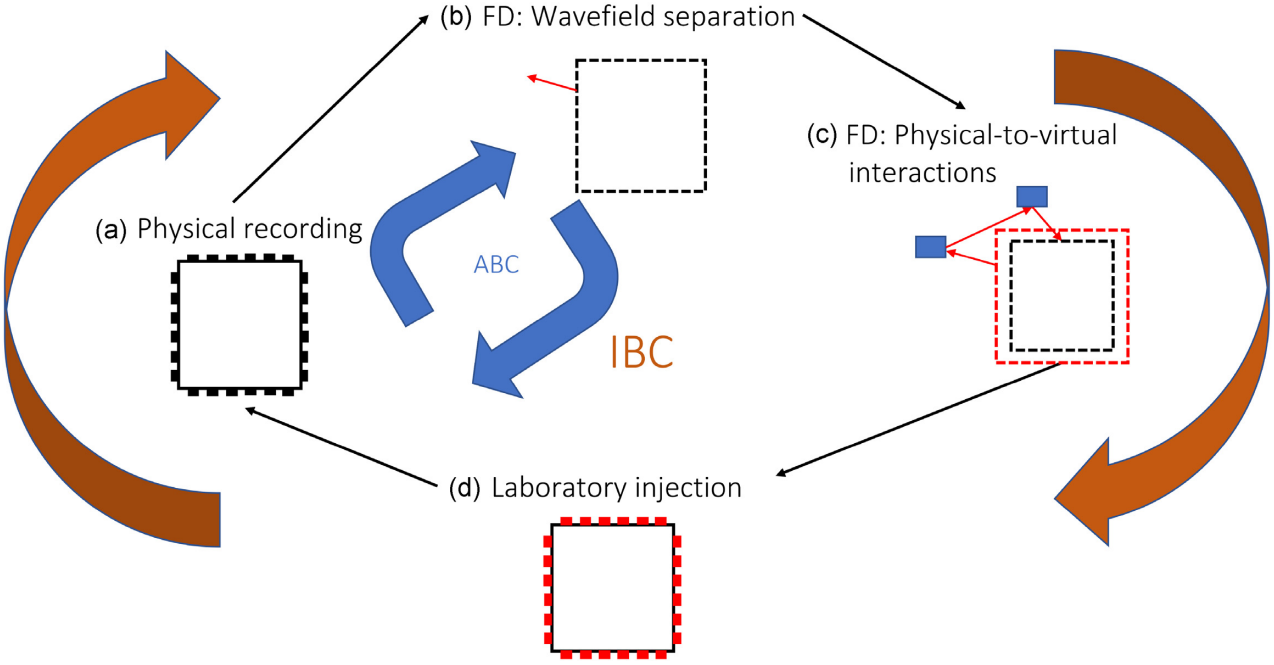

Figure 11. (Colour online) Schematic for illustrating a general iterative structure of the steps as shown, for achieving elastic immersive wave experimentation. (a) Physical recording made at the free surface of a solid experimental domain. (b) FD simulation used for wavefield separation. (c) FD simulation used to compute the wave interaction with a virtual exterior model. (d) Injecting the calculated normal tractions into the physical experiment.

wavefields, wave fronts are shown for primary and secondary waves incident on the free surface from the interior (radiated outward by the wavefield separation), including both *P* and *S* modes (e.g. *pp*, *ps*, *sp* and *ss*). These wave fronts show arrival times that were computed by ray tracing the waves propagating in the homogeneous synthetic wave experiment (first column of Fig. 5). These wavefronts once again confirm that what is obtained using the conventional IABC method is the incident part of all orders of free-surface interactions. Fig. 6(b) shows the normal component of the normal traction vectors, that is, T_z (or namely the τ_{nn} component of $\tau_{ij}\, n_j$) retrieved from the FD simulation for the wavefield separation.

A naive attempt is made to use the normal tractions obtained from the wavefield separation involving the conventional IABC and the windowing approach (Step 3 in Fig. 2) to control the sources deployed at the free surface of the experimental domain. In Fig. 6(b), we separate the primary and higher-order components along the time axis, and the time windows needed are chosen based on the traveltimes of the primary *S* waves from the interior source to the free surface (implicitly assuming a homogeneous medium in between). Fig. 6(c) shows a time–space taper made from the time windows for all receivers or sources on the free surface. Applying this taper to window the retrieved normal tractions [such as in Fig. 6(b)] results in the source signatures used for controlling the boundary sources. Fig. 7 shows this wave experiment, together with a reference simulation performed over an extended homogeneous model. The active boundary condition applied in the experiment results in the cancellation of the unwanted primary outgoing waves (first-order *p and* s) at the early times of the experiment ($t =$ 0.1 and 0.15 ms). Note that in the trace plot of Fig. 7, this wavefield cancellation is shown by the removal of secondary waves (including '*pp*', '*ps*', '*sp*' and '*ss*'), instead of the primary waves, which are recorded as the incident wavefields in the interior of the wave experiment.

However, at later times of the wave experiment (Fig. 7), incorrect waves are generated around the corners of the free surface and propagate into the experimental domain. These waves are caused by the secondary waves, in the FD simulation for the wavefield separation, that are radiated outside the wavefield injection surface S^{sep} immediately after the primary waves of interest, as shown in the second column of Fig. 5. As discussed earlier, any windowing approach is not applicable as the primary and secondary wave arrivals cannot be separated due to their close arrival times [see Fig. 6(d)]. Hence in the wavefield separation (Step 2 in Fig. 2), we instead adapt the IABC method with $d = 10$ cm [Fig. 3(b)]. The third column of Fig. 5 shows the injection of the free-surface data for this IABC compliance. At early times of the FD simulation ($t < 0.2$ ms), the wavefield injection radiates the primary outgoing waves without interference from the secondary waves immediately coming outside the corners of the injection surface S^{sep}. Fig. 6(e) shows the normal traction vector component T_z retrieved from the FD simulation. At later times ($t > 0.2$ ms), higher-order outgoing waves are still radiated out of the planar segments of the injection surface S^{sep} but can be removed using the windowing approach (Step 3 in Fig. 2), resulting in the source signatures (normal tractions) needed for controlling the boundary sources, as shown in Fig. 6(f).

Fig. 8 shows the wave experiment with an active ABC (Step 4 in Fig. 2). Note that some small erroneous wavefields are produced at the top face of the emitting surface S^{emt}, which is caused by the input windowing artefact annotated in Fig. 6(f). This implies that a conservative choice of the time windows is needed in the first cycle of the inner iteration (Step 3). Therefore this artefact can be avoided in the second cycle because removing the first-order *p* wave in the first iteration results in the removal of the secondary *pp* wave, which causes the artefact annotated in Fig. 6(f). Nevertheless, the artefact shown in Fig. 8 is not significant, and we chose not to (re-)carry out the inner iteration.

3.3 Generating first-order physical-to-virtual interaction

Next, we show how Steps 5 and 6 (in Fig. 2) are carried out to produce the first-order physical-to-virtual interaction. In Step 5, outgoing waves that are radiated outside the wavefield injection surface S^{sep} are obtained at the virtual recording surface S^{vrec} (from Step 2), windowed, and then injected into a different FD simulation, which contains the virtual environment and a conventional IABC [Fig. 3(c)]. Fig. 9 shows this injection for the wavefield extrapolation of all primary outgoing waves. In the virtual domain, outgoing waves can interact with the virtual scatterer [defined in Fig. 4(a)], and this interaction is recorded at the locations of the surface S^{sep} for the normal tractions $\tau_{ij}^{\text{vir}} n_j$ as required in eq. (7). Applying the normal tractions $\tau_{ij}^{\text{vir}} n_j$ obtained in Step 5 to the boundary sources can reproduce the ingoing waves (the first-order interaction between the incident outgoing waves and virtual medium), which is shown in Fig. 10 (Step 6).

4 DISCUSSION

The created ingoing waves in Fig. 10 generate new outgoing waves when they are incident on the free surface. Since these new outgoing waves are not taken into account in the current time signatures of the active boundary sources $[\tau_{ij}^{\text{inc}}(\mathbf{x}_{\text{emt}}, t) n_j + \tau_{ij}^{\text{vir}}(\mathbf{x}_{\text{emt}}, t) n_j]$, these waves will reflect and mode convert at the free surface, as shown in Fig. 10. In the next step, therefore one should repeat the inner cycle of the iteration among Steps 2–4 (Fig. 2) to cancel these outgoing waves. For still higher-order interactions between the physical experiment and virtual medium, further iterations of the proposed steps as in Fig. 2 for accumulatively obtaining the term $\tau_{ij}^{\text{hig}}(\mathbf{x}, t) n_j$ as in eq. (7) are required for a complete elastic IBC.

The success of our method for elastic immersive wave experimentation largely relies on the use of IABCs. We apply an adapted IABC to the wavefield separation process (Step 2 in Fig. 2) and a conventional IABC to the wavefield extrapolation process (Step 5). The use of the adapted IABC requires knowledge of the elastic properties within the near-surface part (to depth d) of the solid object, which is necessary for the effective use of the windowing approach (Step 3 in Fig. 2).

If the near-surface part does not involve complex models with strong vertical and lateral heterogeneities, the use of the adapted IABC is feasible in the wavefield separation process. However, an unknown physical scatterer can exist close to the free surface, which must be carefully considered for elastic immersive wave experimentation. One possibility to circumvent this problem involves extending our proposed iterative method into a new iterative method that alternates physical experiments and numerical simulations at each time step of the experiment (instead of using selected time windows). Such a small time step ensures that the recorded free-surface data in each iteration do not contain any higher-order free-surface related multiples. Note that this time stepwise iterative method should share the same two-cycle structure as the iterative method proposed in this paper, and this structure is shown in Fig. 11. This time stepwise method does not need a windowing approach [as it is (pre-)defined] or an internal ABC.

5 CONCLUSION

We propose a novel physical-virtual laboratory that allows immersing a solid wave-physics experiment into a surrounding numerical, virtual medium by deploying a dense set of sources across the boundary of the solid. The theory for such elastic immersive wave experimentation requires the normal tractions of the wavefield at the interface between the physical and virtual domains to control the immersive boundary sources. These normal tractions are derived from the recordings made at the free surface of the solid and the numerical simulations for including physical-to-virtual interactions, by means of an iterative method alternating physical experiments and numerical simulations. Elastic wavefields are first recorded at the free surface of the solid experimental domain, and an iterative scheme involves two cycles of steps: (1) one inner cycle corresponding to cancelling outgoing waves at the free surface of the solid experimental domain and (2) one outer cycle corresponding to generating the waves that represent the interactions between the physical experiment and virtual environment.

In the inner cycle of the iteration, the data recorded at the free surface are injected into an FD simulation with an IABC to separate the outgoing normal tractions. A windowing approach is used to remove unwanted higher-order interactions with the free surface in the normal tractions retrieved from the FD simulation. Such windowed normal tractions act as the time signatures of the sources deployed at the boundary of the physical experiment, forming an active ABC. By iterating the above steps, it is possible to cancel all the primary outgoing waves at the free surface of the physical experiment.

In the outer cycle of the iteration, the outgoing waves separated in the FD simulation are recorded, windowed (for removing unwanted higher-order interactions), and extrapolated within another FD simulation, which contains the virtual medium. The second FD simulation also involves an IABC and outputs the desired normal tractions corresponding to generating the ingoing waves that are scattered by the virtual medium into the physical experiment. Hence, adding the normal tractions obtained from the first and second FD simulations to control the boundary sources creates the first-order physical-to-virtual interaction in a physical wave experiment. The active boundary still needs to cancel the generated (ingoing) waves when they arrive at the free surface, which can be achieved by repeating the inner cycle of the iteration.

We validate the iterative method using 2-D synthetic experiments simulated by means of SEM. The numerical examples confirm that iterating the proposed approaches is necessary for achieving elastic immersive wave experimentation.

ACKNOWLEDGMENTS

This project has received funding from the European Research Council (ERC) under the European Union's Horizon 2020 research and innovation programme (grant agreement no. 694407).

DATA AVAILABILITY

The data and code underlying this paper will be shared on reasonable request to the corresponding author.

REFERENCES

Afanasiev, M., Boehm, C., van Driel, N., Krischer, L., Rietmann, M., May, D.A., Knepley, M.G. & Fichtner, A., 2018. Modular and flexible spectral-element waveform modelling in two and three dimensions, *Geophys. J. Int.*, **216**(3), 1675–1692.

Aki, K. & Richards, P., 2002. *Quantitative Seismology,* Geology University Science Books: Seismology, University Science Books.

Arthur, J.M., Lawton, D.C. & Wong, J., 2012. Physical seismic modeling of a vertical fault, in *SEG Technical Program Expanded Abstracts 2012,* pp. 1–6, Society of Exploration Geophysicists, Tulsa, Oklahoma, US.

Becker, T.S. *et al.*, 2018. Immersive wave propagation experimentation: physical implementation and one-dimensional acoustic results, *Phys. Rev. X,* **8**(3), 031011, doi:10.1103/PhysRevX.8.031011.

Becker, T.S., Börsing, N., Haag, T., Bärlocher, C., Donahue, C.M., Curtis, A., Robertsson, J. O.A. & van Manen, D.-J., 2020. Real-time immersion of physical experiments in virtual wave-physics domains, *Phys. Rev. Appl.,* **13**(6), 064061, doi:10.1103/PhysRevApplied.13.064061.

Berkhout, A.J., de Vries, D. & Vogel, P., 1993. Acoustic control by wave field synthesis, *J. acoust. Soc. Am.,* **93**(5), 2764–2778.

Börsing, N., Becker, T.S., Curtis, A., van Manen, D.-J., Haag, T. & Robertsson, J.O., 2019. Cloaking and holography experiments using immersive boundary conditions, *Phys. Rev. Appl.,* **12**(2), 024011, doi:10.1103/PhysRevApplied.12.024011.

Brenders, A.J. & Pratt, R.G., 2007. Full waveform tomography for lithospheric imaging: results from a blind test in a realistic crustal model, *Geophys. J. Int.,* **168**(1), 133–151.

Bretaudeau, F., Leparoux, D., Durand, O. & Abraham, O., 2011. Small-scale modeling of onshore seismic experiment: a tool to validate numerical modeling and seismic imaging methods, *Geophysics,* **76**(5), T101–T112.

Cheer, J., 2016. Active control of scattered acoustic fields: cancellation, reproduction and cloaking, *J. acoust. Soc. Am.,* **140**(3), 1502–1512.

Craster, R. & Guenneau, S., 2012. *Acoustic Metamaterials: Negative Refraction, Imaging, Lensing and Cloaking,* Springer Series in Materials Science, Springer Netherlands.

Cui, T., Vasconcelos, I., Manen, D.-J.v. & Wapenaar, K., 2018. A tour of Marchenko redatuming: focusing the subsurface wavefield, *Leading Edge,* **37**(1), 67a1–67a6.

Derode, A., Roux, P. & Fink, M., 1995. Robust acoustic time reversal with high-order multiple scattering, *Phys. Rev. Lett.,* **75,** 4206–4209.

Fichtner, A., 2010. *Full Seismic Waveform Modelling and Inversion, Advances in Geophysical and Environmental Mechanics and Mathematics,* Springer Berlin Heidelberg.

Guyer, R.A. & Johnson, P.A., 2009. *Nonlinear Mesoscopic Elasticity: The Complex Behaviour of Rocks, Soil, Concrete,* Wiley, New York.

Hadziioannou, C., Larose, E., Coutant, O., Roux, P. & Campillo, M., 2009. Stability of monitoring weak changes in multiply scattering media with ambient noise correlation: laboratory experiments, *J. acoust. Soc. Am.,* **125**(6), 3688–3695.

Igel, H., 2017. *Computational Seismology: A Practical Introduction,* Oxford University Press.

King, M., 2002. Elastic wave propagation in and permeability for rocks with multiple parallel fractures, *Int. J. Rock Mech. Mining Sci.,* **39**(8), 1033–1043.

Larose, E., Planes, T., Rossetto, V. & Margerin, L., 2010. Locating a small change in a multiple scattering environment, *Appl. Phys. Lett.,* **96**(20), 204101, doi:10.1063/1.3431269.

Li, X., Koene, E., van Manen, D.-J., Robertsson, J. & Curtis, A., 2022a. Elastic immersive wavefield modelling, *J. Comput. Phys.,* **451,** 110826, doi:10.1016/j.jcp.2021.110826.

Li, X., Robertsson, J., Curtis, A. & van Manen, D.-J., 2022b. Internal absorbing boundary conditions for closed-aperture wavefield decomposition in solid media with unknown interiors, *J. acoust. Soc. Am.,* **152**(1), 313–329.

McDonald, J., Gardner, G. & Hilterman, F., 1983. *Seismic Studies in Physical Modeling,* Springer, The Netherlands.

Mikesell, D. & van Wijk, K., 2011. Seismic refraction interferometry with a semblance analysis on the crosscorrelation gather, *Geophysics,* **76**(5), SA77–SA82.

Nosjean, N., Khamitov, Y., Rodriguez, S. & Yahia-Cherif, R., 2020. Fracture corridor identification through 3D multifocusing to improve well deliverability, an Algerian tight reservoir case study, *Solid Earth Sci.,* **5**(1), 31–49.

Park, C.M. & Lee, S.H., 2019. Zero-reflection acoustic metamaterial with a negative refractive index, *Sci. Rep.,* **9**(1), 3372, doi:10.1038/s41598-019-40184-7.

Pendry, J.B., 2000. Negative refraction makes a perfect lens, *Phys. Rev. Lett.,* **85,** 3966–3969.

Pinto, P., Sousa, A. & Bizarro, P., 2018. Incorporating rock physics in fracture characterization and modelling: a conceptual workflow from a carbonate reservoir, *Eur. Assoc. Geosci. Eng.,* **2018**(1), 209–212.

Qi, C., Kohlstedt, D.L., Katz, R.F. & Takei, Y., 2015. Experimental test of the viscous anisotropy hypothesis for partially molten rocks, *Proc. Natl. Acad. Sci.,* **112**(41), 12616–12620.

Robertsson, J.O., van Manen, D.-J., Schmelzbach, C., Van Renterghem, C. & Amundsen, L., 2015. Finite-difference modelling of wavefield constituents, *Geophys. J. Int.,* **203**(2), 1334–1342.

Sivaji, C., Nishizawa, O., Kitagawa, G. & Fukushima, Y., 2002. A physical-model study of the statistics of seismic waveform fluctuations in random heterogeneous media, *Geophys. J. Int.,* **148**(3), 575–595.

Snieder, R., 2002. General theory of elastic wave scattering, in *Scattering,* pp. 528–542, Academic Press.

Snieder, R., Grêt, A., Douma, H. & Scales, J., 2002. Coda wave interferometry for estimating nonlinear behavior in seismic velocity, *Science,* **295**(5563), 2253–2255.

Tarantola, A., 1984. Inversion of seismic reflection data in the acoustic approximation, *Geophysics,* **49**(8), 1259–1266.

Thomsen, H.R., Molerón, M., Haag, T., van Manen, D.-J. & Robertsson, J. O.A., 2019. Elastic immersive wave experimentation: Theory and physical implementation, *Phys. Rev. Res.,* **1**(3), 033203, doi:10.1103/PhysRevResearch.1.033203.

Thomsen, H.R., Koene, E.F.M., Robertsson, J.O.A. & van Manen, D.-J., 2021. FD-injection-based elastic wavefield separation for open and closed configurations, *Geophys. J. Int.,* **227**(3), 1646–1664.

Tsvankin, I., 2012. *Seismic Signatures and Analysis of Reflection Data in Anisotropic Media,* Geophysical References Series, Society of Exploration Geophysicists.

van Manen, D.-J., Curtis, A. & Robertsson, J.O., 2006. Interferometric modeling of wave propagation in inhomogeneous elastic media using time reversal and reciprocity, *Geophysics,* **71**(4), SI47–SI60.

van Manen, D.-J., Robertsson, J. O.A. & Curtis, A., 2007. Exact wave field simulation for finite-volume scattering problems, *J. acoust. Soc. Am.,* **122**(4), EL115–EL121.

Vasmel, M., Robertsson, J.O., van Manen, D.-J. & Curtis, A., 2013. Immersive experimentation in a wave propagation laboratory, *J. acoust. Soc. Am.,* **134**(6), EL492–EL498.

Virieux, J., 1986. P-SV wave propagation in heterogeneous media: Velocity-stress finite-difference method, *Geophysics,* **51**(4), 889–901.

Wapenaar, K. & Fokkema, J., 2006. Green's function representations for seismic interferometry, *Geophysics,* **71**(4), SI33–SI46.

Wapenaar, K., Broggini, F., Slob, E. & Snieder, R., 2013. Three-dimensional single-sided marchenko inverse scattering, data-driven focusing, green's function retrieval, and their mutual relations, *Phys. Rev. Lett.,* **110**(5), 084301, doi:10.1103/PhysRevLett.110.084301.

Wapenaar, K., Thorbecke, J., van der Neut, J., Broggini, F., Slob, E. & Snieder, R., 2014. Marchenko imaging, *Geophysics,* **79**(3), WA39–WA57.

Williams, J. E.F., 1984. Review lecture - anti-sound, *Proc. R. Soc. London. A. Math. Phys. Sci.,* **395**(1808), 63–88.

Wong, Z.J. *et al.*, 2017. Optical and acoustic metamaterials: superlens, negative refractive index and invisibility cloak, *J. Optics,* **19**(8), 084007, doi:10.1088/2040-8986/aa7a1f.

Yang, L.-T., Li, X., Yu, H.-S. & Wanatowski, D., 2016. A laboratory study of anisotropic geomaterials incorporating recent micromechanical understanding, *Acta Geotech.,* **11**(5), 1111–1129.

APPENDIX A: DERIVING ELASTIC REPRESENTATION THEOREMS

In this appendix, we derive the representation theorems for an immersive wave environment and a physical experiment without any sources deployed at the boundary, following Vasmel *et al.* (2013). We first consider expressing the particle velocity wavefield in an extended, full domain [e.g. Fig. 1(b)] in terms of an auxiliary state

Table A1. Source fields and medium properties of states A and B.

	State A	State B
Wavefields	$v_i^A(\mathbf{x})$, $\tau_{ij}^A(\mathbf{x})$	$v_i^B(\mathbf{x}) = G_{i,n}^{v,f}(\mathbf{x}, t \mid \mathbf{x}_b, 0)$, $\tau_{ij}^B(\mathbf{x}) = G_{ij,n}^{\tau,f}(\mathbf{x}, t \mid \mathbf{x}_b, 0)$
Sources	$f_i^A(\mathbf{x}, t) \neq 0$ for $\mathbf{x} \in V$	$f_i^B(\mathbf{x}, t) = \delta(t)\delta(\mathbf{x} - \mathbf{x}_b)\delta_{in}$
	$h_{kl}^A(\mathbf{x}, t) = 0$	$h_{kl}^B(\mathbf{x}, t) = 0$
Medium	$c_{ijkl}^A(\mathbf{x}) = c_{ijkl}^B(\mathbf{x})$, $\rho^A(\mathbf{x}) = \rho^B(\mathbf{x})$ for $\mathbf{x} \in V$	
Boundary condition	Sommerfeld on S	$\tau_{ij}^B(\mathbf{x}, t)n_j = 0$ for $\mathbf{x} \in S$

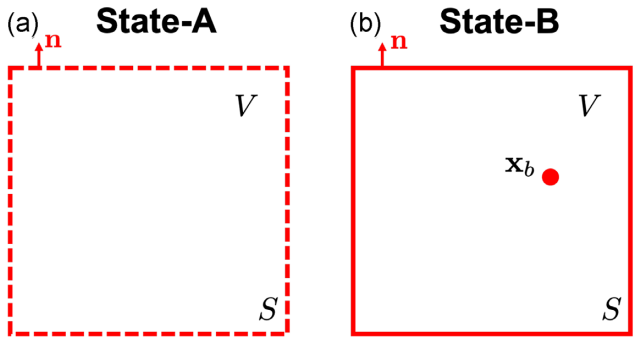

Figure A1. (Colour online) (a) State A: the volume V is enclosed by the transparent surface S (dashed red square) with normal vector $\mathbf{n}$. (b) State B: an impulsive body force source is placed at $\mathbf{x}_b$ (red dot) inside V. The surface S is a reflecting free surface (solid red square).

bounded by a traction-free boundary [e.g. Fig. 1(a)]. We define two states, A and B, of wave propagation as illustrated in Fig. A1, with their definitions given in Table A1. The two states correspond to two independent sets of wave equations of the form as in eqs (1) and (2), which are connected using the so-called interaction quantity: $\partial(\tau_{ij}^A * v_i^B - \tau_{ij}^B * v_i^A)/\partial x_j$ where the symbol $*$ denotes temporal convolution. This quantity is further integrated over the volume V (see Fig. A1), and applied with the divergence theorem of Gauss [i.e. $\iiint \nabla \cdot \mathbf{F}\, \mathrm{d}V = \iint \mathbf{F} \cdot \mathbf{n}\, \mathrm{d}S$ where $\mathbf{F} = (\tau_{ij}^A * v_i^B - \tau_{ij}^B * v_i^A)$]:

$$\iiint_V \partial_j \left(\tau_{ij}^A * v_i^B - \tau_{ij}^B * v_i^A\right) \mathrm{d}V = \oint_S \left(\tau_{ij}^A * v_i^B - \tau_{ij}^B * v_i^A\right) n_j \, \mathrm{d}S \tag{A1}$$

where n_j is the normal vector component of S enclosing V. We further replace the terms inside of the volume integral on the left-hand side of eq. (A1) with the wave equations for states A and B, and use the fact about medium properties: $c_{ijkl}^A(\mathbf{x}) = c_{ijkl}^B(\mathbf{x})$, $\rho^A(\mathbf{x}) = \rho^B(\mathbf{x})$ for $\mathbf{x}$ located inside V, to simplify the volume integral, which gives (Wapenaar & Fokkema 2006)

$$\iiint_V \left(\tau_{ij}^A * h_{ij}^B + v_i^A * f_i^B - \tau_{ij}^B * h_{ij}^A - v_i^B * f_i^A\right) \mathrm{d}V = \oint_S \left(\tau_{ij}^A * v_i^B - \tau_{ij}^B * v_i^A\right) n_j \, \mathrm{d}S \tag{A2}$$

Eq. (A2) is called a reciprocity theorem of the convolution type (Aki & Richards 2002; van Manen *et al.* 2006).

We further incorporate the source definitions and boundary conditions for states A and B (see Table A1) into both the volume and surface integrals of eq. (A2), resulting in

$$v_n^A - \iiint_V v_i^B * f_i^A \, \mathrm{d}V = \oint_S \left(\tau_{ij}^A n_j\right) * v_i^B \, \mathrm{d}S \tag{A3}$$

Note that state A involves a Sommerfeld radiation boundary condition over the surface S (i.e. a transparent surface) while state B involves a free surface across S: $\tau_{ij}^B(\mathbf{x}, t)n_j = 0$ for $\mathbf{x} \in S$. State B involves an impulsive point source and is hence also called a Green's state in which elastic wavefields can be expressed as Green's functions (van Manen *et al.* 2006). Then eq. (A3) is recast as

$$v_n^A(\mathbf{x}_b, t) = \int G_{i,n}^{v,f}(\mathbf{x}, t \mid \mathbf{x}_b, 0) * f_i^A(\mathbf{x}, t) \, \mathrm{d}V(\mathbf{x}) + \oint_S G_{i,n}^{v,f}(\mathbf{x}, t \mid \mathbf{x}_b, 0) * \tau_{ij}^A(\mathbf{x}, t) n_j \, \mathrm{d}S(\mathbf{x}) \tag{A4}$$

where the Green's function $G_{n,i}^{v,f}(\mathbf{x}, t \mid \mathbf{x}_b, 0)$ represents the particle velocity (superscript v) in the n direction (x_n) recorded at the location $\mathbf{x}$ due to an impulsive point source of body force (f) in the i direction (x_i) at the location $\mathbf{x}_b$.

We proceed by applying elastic source-receiver reciprocity, that is, $G_{i,n}^{v,f}(\mathbf{x}, t \mid \mathbf{x}_b, 0) = G_{n,i}^{v,f}(\mathbf{x}_b, t \mid \mathbf{x}, 0)$ to eq. (A4) (Snieder 2002), which then becomes

$$v_n^A(\mathbf{x}_b, t) = \int G_{n,i}^{v,f}(\mathbf{x}_b, t \mid \mathbf{x}, 0) * f_i^A(\mathbf{x}, t) \, \mathrm{d}V(\mathbf{x}) + \oint_S G_{n,i}^{v,f}(\mathbf{x}_b, t \mid \mathbf{x}, 0) * \tau_{ij}^A(\mathbf{x}, t) n_j \, \mathrm{d}S(\mathbf{x}) \tag{A5}$$

eq. (A5) is the elastic representation theorem of the convolution type, which allows expressing the particle velocity wavefield v_n^A in the full, extended domain in terms of (1) the Green's functions in the truncated, original physical domain, (2) the source term f_i^A in the extended domain and (3) the normal tractions $\tau_{ij}^A n_j$ at the transparent interface between the physical and virtual parts of the full domain. For an elastic immersive wave experiment shown in Fig. 1(a), the representation theorem, eq. (A5), can be reformatted as eq. (3) in the main text. Subsequently, we need to find an expression for a physical experiment without exciting boundary sources [Fig. 3(a)]. Here, we further modify state A by setting the surface S to be a reflecting free surface [$\tau_{ij}^A(\mathbf{x}_S, t)n_j = 0$], and settings for auxiliary state B stay the same as before. In this case, the normal traction term $\tau_{ij}^A(\mathbf{x}, t)n_j$ in eq. (A5) becomes zero, which gives:

$$v_n^A(\mathbf{x}_b, t) = \int G_{n,i}^{v,f}(\mathbf{x}_b, t \mid \mathbf{x}, 0) * f_i^A(\mathbf{x}, t) \, \mathrm{d}V(\mathbf{x}) \tag{A6}$$

which corresponds to eq. (4) in the main text.

APPENDIX B: RETRIEVING NORMAL TRACTIONS IN FINITE-DIFFERENCE SIMULATIONS FOR WAVEFIELD SEPARATION

In Step 2 of the iterative method (Fig. 2), the FD simulation should output the normal tractions of the outgoing waves, which are radiated outside the wavefield injection surface S^{sep}. In this scenario, outgoing normal tractions were considered to be retrieved possibly only outside the surface S^{sep}, namely at least one FD gridpoint away from S^{sep} (Thomsen *et al.* 2021). However, in theory, the locations of

the separated wavefields should be exactly at the wavefield injection surface S^{sep}. One way to fill this gap is to extrapolate or redatum the separated outgoing wavefields obtained outside the injection surface S^{sep} back to S^{sep} (Robertsson *et al.* 2015). Nevertheless, we find that the desired normal traction vector $\tau_{ij}n_j$ can be obtained directly at the wavefield injection surface S^{sep} in the FD simulation.

A free surface in a physical experiment implies that the normal tractions across the surface are always zero except at the locations where boundary sources are excited (Wapenaar & Fokkema 2006):

$$[\tau_{ij}n_j]^{\text{free}} = 0 \tag{B1}$$

At the free surface, the total normal tractions are the sum of those due to the incident, outgoing waves and those due to the reflected ingoing waves:

$$[\tau_{ij}n_j]^{\text{out}} + [\tau_{ij}n_j]^{\text{in}} = 0 \tag{B2}$$

In the FD simulation for the wavefield separation, outgoing waves are reconstructed with opposite polarity while ingoing waves have correct polarity (Robertsson *et al.* 2015). This implies that outgoing wave energy attributes the normal tractions $-[\tau_{ij}n_j]^{\text{out}}$ to the injection surface S^{sep} while ingoing wave energy attributes the normal tractions $[\tau_{ij}n_j]^{\text{in}}$. In the FD simulation, we consider that the normal tractions at the injection surface S^{sep}, simultaneously with the wavefield injection, are the average of the tractions due to the reconstructed out- and ingoing waves:

$$[\tau_{ij}n_j]^{\text{sep}} = \left([\tau_{ij}n_j]^{\text{in}} - [\tau_{ij}n_j]^{\text{out}}\right)/2 \tag{B3}$$

Substituting eq. (B2) into eq. (B3) gives

$$[\tau_{ij}n_j]^{\text{sep}} = -[\tau_{ij}n_j]^{\text{out}} \tag{B4}$$

Hence in theory, the normal tractions of the separated outgoing waves can be obtained directly at the wavefield injection surface S^{sep}. In the FD simulation for wavefield separation, a practice is to first carry out the wavefield injection at the surface S^{sep} and then extract the normal tractions across S^{sep}.